Flexural excitation in a standard torsional-resonant column device

Giovanni Cascante, Carlos Santamarina, and Najwa Yassir

Abstract: The excitation of specimens in multiple modes enhances the characterization of granular materials. The purpose of this paper is to present the equipment modification and test procedure and data reduction for flexural excitation in a standard torsional-resonant column device. Typical results for dry and wet sand specimens are also presented. A salient advantage of the modified device is that it permits testing shear stiffness (torsional excitation) and longitudinal stiffness (flexural excitation) at frequencies which are relevant to high-resolution seismics and near-surface studies (approx. 50–200 Hz). High attenuation in flexural mode is measured in saturated and partially saturated specimens; local flow is suspected as a prevailing loss mechanism. Velocity and damping ratios are complementary indicators of saturation conditions prevailing in the specimen.

Key words: mechanical waves, resonant column, velocity, attenuation, sands, modal testing.

Résumé : L'excitation de spécimens en modes multiples améliore la caractérisation des matériaux pulvérulents. Le but de cet article est de présenter la modification de l'appareil, la procédure de l'essai et la réduction des données pour l'excitation en flexion dans un appareil standard de torsion à colonne résonnante. L'on présente aussi des résultats typiques pour des spécimens de sable sec et humide. Un avantage certain de cet appareil modifié est qu'il permet de mesurer la rigidité en cisaillement (excitation en torsion) et la rigidité longitudinale (excitation en flexion) à des fréquences qui sont applicables à des études de séismicité à haute-résolution et près de la surface (approximativement de 50 à 200 Hz). Une forte atténuation dans le mode en flexion est mesurée dans les spécimens saturés et partiellement saturés; l'on soupçonne qu'un écoulement local est le mécanisme dominant de rupture. Les rapports de vitesse et d'amortissement sont des indicateurs des conditions de saturation qui prédominent dans le spécimen.

Mots clés : ondes mécaniques, colonne résonnante, vitesse, atténuation, sables, mode d'essai.

[Traduit par la Rédaction]

Introduction

The study of particulate materials with longitudinal and transverse wave propagation provides complementary information about fabric, state of stress, and fluid–skeleton interaction without altering the fabric or causing permanent effects. Furthermore, wave parameters determined in the laboratory under different excitation modes can be used to compute parameters applicable to other propagation modes in the field (Fratta and Santamarina 1996).

Changes in lithology can be estimated from the ratio of P-wave to S-wave velocities V_P/V_S. This ratio reflects changes in porosity, clay content, and the aspect ratio of pores (Toksöz et al. 1976; Domenico and Danbom 1987; Eastwood and Castagna 1987). Inelastic attenuation may cause V_P/V_S to be frequency dependent. Damping adds additional information: if the ratio of the compressional damping to the shear damping coefficient D_P/D_S is greater than unity, V_P/V_S decreases with increasing frequency (Futterman 1962; Eastwood and Castagna 1987). Hence, the determination and analysis of attenuation in multimode wave propagation studies can enhance the state of the art in stratigraphic and lithologic evaluations (Dutta 1987).

Attenuation and dispersion for strains less than 10^{-6} is controlled by the degree of fluid saturation and the frequency content of the wave (Winkler and Nur 1982). Mathematical models are available to predict wave velocity and attenuation in porous media with isolated or interconnected pore spaces, with the general assumption that macrofluid flow does not develop as the wave propagates through the medium. Most studies have been conducted in rocks using high-frequency waves (frequency of excitation $f > 1$ kHz). Experimental results in sandstones and porous glass showed that D_S/D_P is greater than unity for full water saturation, but it is less than unity for partial saturation. Apparently, the large compressibility of the gas–water mixture enhances fluid-flow mechanisms in the compressional mode (Murphy 1982; White 1975).

This paper presents the modification of a standard resonant column to determine velocity and attenuation in specimens subjected to flexural and torsional excitations. The modified device is used to conduct an exploratory study of the effect of saturation on low-strain wave velocity and attenuation. The operating frequency (between 50 and 200 Hz)

Received February 7, 1997. Accepted January 20, 1998.

G. Cascante. Department of Civil Engineering, University of Waterloo, Waterloo, ON N2L 3G1, Canada. e-mail: gcascant@uwaterloo.ca
C. Santamarina. Department of Civil and Environmental Engineering, Georgia Institute of Technology, Atlanta, GA 30332-0355, U.S.A. e-mail: carlos@ce.gatech.edu
N. Yassir. CSIRO Petroleum, Victoria 3150, Australia. e-mail: n.yassir@dpr.csi

Table 1. Experimental conditions: chronology.

Specimen and sequence	Void ratio e	Mass density ρ (kN s^2/m^4)	Degree of saturation S_r (%)	Effective stress σ_o' (kPa)
1 (na)	0.50	1.77	0.01	27–400
2 (I)	0.50	2.10	100	35–408
2 (II)	0.50	2.10	100 (back pressure)	41–203
2 (III)	0.50	1.90	41	55–413

Fig. 1. Resonant column device. LVDT, linear voltage displacement transducer. (A) Instrumentation. (B) Torsional and flexural excitation.

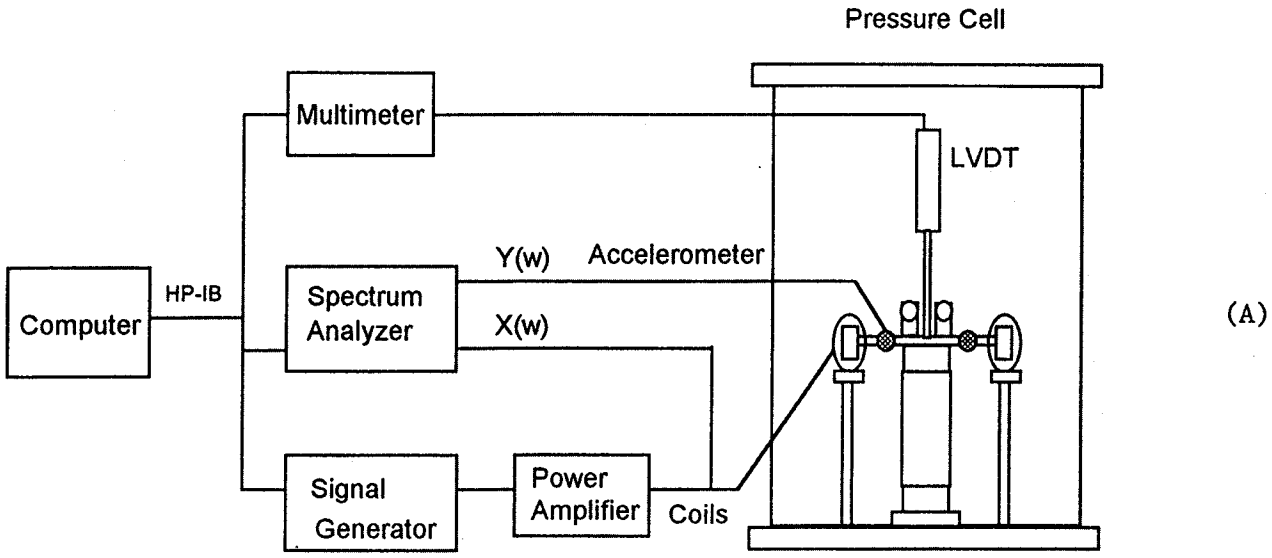

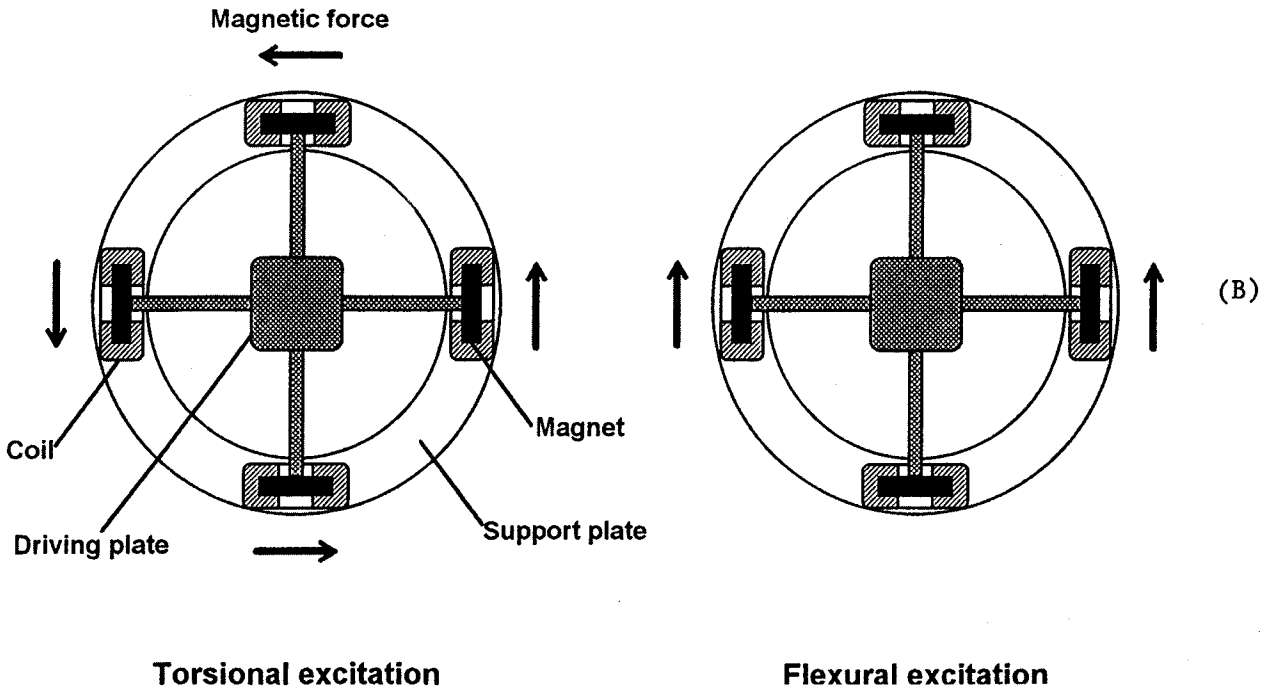

Table 2. Summary of test results.

Specimen No.	Test condition S_r (%)	Exponent b_S	Exponent b_{LF}	Damping ratio D_F/D_S (Hz)	Resonant frequency Torsion (Hz)	Resonant frequency Flexion (Hz)
1	Dry	0.25	0.25	1.0	90–175	50–101
2	100 (no back pressure)	0.26	0.24	3.0	100–187	55–99
2	100 (with back pressure)	0.25	0.23	2.5	105–160	61–86
2	41 (no back pressure)	0.24	0.21	2.5	115–189	65–101

approaches the frequency range used in near-surface geophysical studies. Device modification and calibration, test procedure, and relevant equations for data analysis are presented first, followed by experimental results and discussion.

Device modification and calibration

The resonant column torsional shear device is a laboratory apparatus specifically designed to measure dynamic properties of soils for shear strains between 10^{-6} and 10^{-2}. The resonant test is essentially nondestructive, therefore the dynamic properties can be evaluated at different confining pressures for each soil specimen. The small shear strain produced with the resonant column apparatus is in the same order of magnitude as that of geophysical in situ tests.

Device

A resonant column for torsional excitation (Stokoe cell SBEL D1128) was modified to excite both the torsional and the flexural vibration modes. The test is run with a signal analyzer. The input signal is a narrow band random noise. The resonant frequency and damping ratio were computed by curve-fitting the frequency response obtained with average cross and auto spectra between the excitation coils and the response of accelerometer (Fig. 1A). This procedure is more robust than the one-point estimation based on resonance, or the three-point "half power" estimator (Cascante and Santamarina 1997).

Transverse excitation was imposed with the same set of magnets and coils used in torsional excitation. In the original configuration, the coils are connected in series to produce a net torque at the top of the specimen (Fig. 1B). In the modified configuration, the coils are reconnected to produce a net horizontal force at the top of the specimen (Fig. 1B). The type of excitation can be selected with a switch outside the chamber, without introducing any perturbation to the specimen and its stress history.

The low-strain Young's modulus computed from flexural and longitudinal excitation is the same in single-phase materials. However, this is not the case in water-bearing particulate materials because of differences in fluid–matrix interaction in flexural and longitudinal excitations. A special top cap was built to facilitate saturation. It includes a concentric valve to avoid the effect of eccentric masses on torsional excitation. Before testing, the valve is closed and the tube used for saturation is disconnected and removed.

Analysis

The free vibration analysis for a cantilever beam of length L with a rigid mass at the free end indicates that the first resonant frequency of the flexural mode ω_f depends on the position of the rigid mass. The following equation is obtained using Rayleigh's method and considering N distributed masses m_i (Cascante 1996):

$$[1] \qquad \omega_f^2 = \frac{3EI_b}{L^3\left[\frac{33}{140}m_T + \sum_{i=1}^{N} m_i h(h0_i, h1_i)\right]}$$

where

$$[2] \qquad h(h0_i, h1_i) = m_i\left[1 + 3\frac{(h1_i + h0_i)}{2L} + \frac{3}{4}\left(\frac{h1_i^2 + h1_i h0_i + h0_i^2}{L}\right)^2\right]$$

$h0_i$ and $h1_i$ are the heights at the bottom and the top, respectively, of mass i, measured from the top of the soil specimen; and E, I_b, and m_T are Young's modulus, area moment of inertia, and mass of the specimen, respectively. Equation [1] can be expressed in terms of the center of gravity y_{ci} and the area moment of inertia with respect to the center of gravity I_{yi} of each mass m_i:

$$[3] \qquad \omega_f^2 = \frac{3EI_b}{L^3\left[\frac{33}{140}m_T + \sum_{i=1}^{N} m_i + \frac{3m_i y_{ci}}{L} + \frac{9(I_{yi} + m_i y_{ci})}{4L^2}\right]}$$

The derivations of eqs. [1]–[3] are presented in Appendix 2. Equation [3] assumes that the confinement is higher than the maximum axial stress induced by the flexural excitation. Therefore, no tension is applied to the soil specimen.

Calibration

The mass, center of gravity, and area moment of inertia of the driving plate and top cap are needed. In general, due to the complex geometry of the driving system and top cap, the experimental determination of the area moment of inertia I_y is preferred. A metal calibration specimen and a calibration mass are used to measure I_y using eq. [3]. The step-by-step calibration procedure follows (it parallels the calibration procedure conducted for the torsional mode):

(1) Measure the resonant frequency of the calibration specimen alone, ω_1.

(2) Measure the resonant frequency of the calibration specimen with the added calibration mass at the top, ω_2.

(3) Compute with eq. [2] the equivalent height of the calibration mass h_a and the height of the top bar of the calibration specimen h_b.

(4) Set a system of two equations and two unknowns using eq. [3] and parameters ω_1, ω_2, h_a, and h_b. Solve for the area moment of inertia of the driving plate I_{yp} and the flexural stiffness of the calibration specimen $3EI_b/L^3$, assuming that the center of gravity of the driving plate is at its geometrical center.

(5) Confirm the computed values by changing the vertical position of the driving plate.

(6) The new flexural stiffness, computed with the measured frequency ω_3 and the new equivalent height of the driving plate, must agree with values computed in step 4.

(7) If the geometry of the top cap is too complex to use eq. [2], measure its mass moment of inertia following the previous steps once that I_{yp} is known.

The area moment of inertia of the driving system I_{yp} must be recalibrated whenever new transducers are added or modifications are implemented. Likewise, eq. [3] has to be recomputed when masses are added to the top cap or when the position of masses is changed. Errors in the position of masses and on the measurement of the specimen's height have a significant effect on the computation of Young's modulus E and the longitudinal wave velocity V_{LF}; for example, a 5% error in the position of the driving plate or in the specimen's height can produce a 20% error in the computed wave velocity.

Longitudinal versus flexural excitation

The resonant frequency of a cantilever beam gives an accurate method of measuring Young's modulus from flexural excitation E_{flex} (eq. [3]) (Kolsky 1963). The longitudinal wave velocity V_{LF} in a rod can be calculated from E_{flex} and the density of the specimen ρ:

$$[4] \qquad V_{LF} = \frac{\sqrt{E_{flex}}}{\rho}$$

This relation presumes that the wavelength is significantly longer than the diameter of the bar and any internal scale in the material (e.g., particle size).

There are significant differences between the strain field induced in a specimen excited in flexural and longitudinal modes. The former has a triangular-Navier variation of strain in the cross section, from tension to compression, whereas the latter has a constant strain distribution in a given cross section. In addition, the axial strain in a cantilever beam with a transverse load at the free end varies linearly along the longitudinal axis.

Wave-propagation parameters depend on the maximum strain imposed. For the torsional mode, the maximum volume – average shear strain is considered representative. Following the same criterion, the maximum volume – average axial strain ε_{avg} for the flexural vibration mode is

$$[5] \qquad \varepsilon_{avg} = \frac{2}{3\pi}\varepsilon_{max}$$

where

$$[6] \qquad \varepsilon_{max} = \frac{volt_{pk} Rg}{4\pi SL^2 f^2}$$

$volt_{pk}$ is the maximum output voltage of the accelerometer (in mV); R and L are the radius and length of the specimen, respectively (in cm); g is the acceleration due to gravity (in cm/s^2); S = 99.2 mV/g is the sensitivity of the accelerometer; and f is the flexural resonant frequency (in Hz). Equation [5] is derived in Appendix 2. Equation [6] assumes a pure flexural motion; this can be verified with two accelerometers mounted on the driving plate. The volume change $|\Delta vol|$ in either the tension side or the compression side of the specimen is

$$[7] \qquad |\Delta vol| = \frac{1}{3} R^2 L \varepsilon_{max}$$

The instantaneous pore-pressure distribution in saturated specimens reflects the variations in strain field. The pressure gradient in longitudinal vibration is parallel to the vertical axis of the specimen. Hence, fluid flow in Biot's wave of the second type is out of phase with the solid matrix but in the same direction. However, the pressure gradient is almost horizontal in flexural vibration and the liquid tends to move perpendicular to the motion of the solid matrix.

The form of interaction between the fluid and the matrix affects wave velocity and attenuation. If the rate of pore-pressure dissipation from diametrically opposed regions in the specimen is greater than the period of vibration of the flexural mode, the longitudinal velocity from the flexural mode V_{LF} is governed by the compressional stiffness of the matrix, even in saturated media.

The estimated volume of mobilized water due to the elastic deformation of the soil skeleton in this study is about 0.04 cm^3 (corresponds to $\varepsilon_{max} = 10^{-5}$, eq. [7]). This volume is small enough to be accommodated at the membrane soil–pore interface. Then, the excess pore pressure caused by either longitudinal or flexural excitation would decay towards the membrane (transverse flow in both excitations). The effect of membrane compliance is maximized at low frequencies, and the compressional stiffness of the fluid would not contribute to the P-wave velocity.

Experimental study and results

Tests with the modified resonant column were designed to study shear wave parameters and longitudinal wave parameters in sand specimens under isotropic loading and different moisture conditions. Two dense specimens were prepared, one for the air-dry test and one for the wet tests (saturated and partially saturated conditions) and tested at low strain levels (axial and shear strains $<10^{-5}$).

Specimen preparation

A uniform silica sand was used in this study (Barco sand 32, diameter for 50% passing D_{50} = 0.44 mm, maximum void ratio e_{max} = 0.73, minimum void ratio e_{min} = 0.49, specific gravity of soil G_s = 2.65). Specimens were prepared by the dry-pluviation technique and tamping every 2 cm to obtain a dense specimen and to minimize the effects of changes in void ratio during testing (relative density $D_r \approx$ 100%, specimen length L = 13.6 cm, diameter d = 7.1 cm).

Fig. 2. Dry specimen: torsional excitation. (A) Stress–strain curve and SC packing model. (B) Shear wave velocity V_S vs. confinement. (C) Damping D_S vs. confinement.

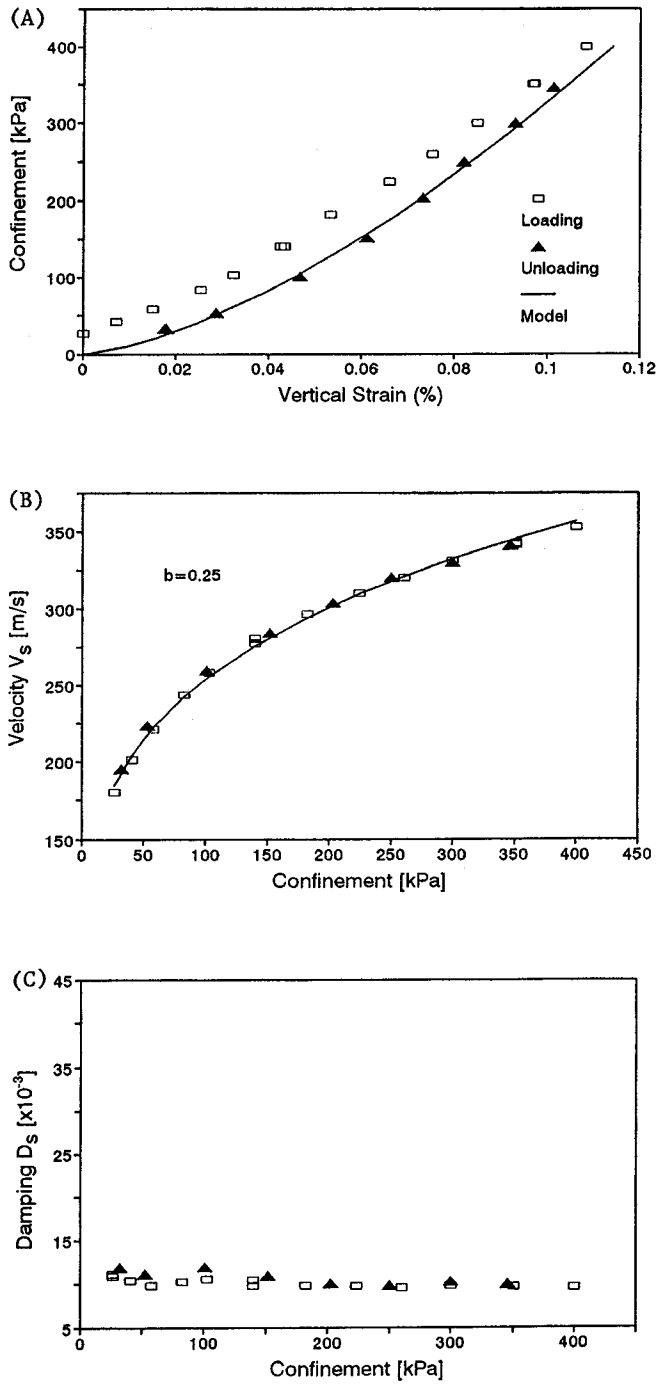

Once the upper platen was set in place, vacuum was applied to hold the specimen in place, and the split mold was removed. The wet specimen was prepared by allowing water flow from bottom to top, first under capillary and gravitational forces and second by applying vacuum (15 cm of mercury), before the split mold was removed. The dry specimen was confined with air. The wet specimen was surrounded by a water-filled cylinder to maintain saturation conditions.

Test sequences

The confining pressure was increased in stages. Each load increment was maintained until all microseismic events ended (10–30 min). Torsional and flexural resonant frequencies and damping coefficients were measured at each load stage. The air-dry specimen was isotropically loaded from 27 to 400 kPa. Three tests were performed on the wet specimen: (1) increase in effective isotropic confinement from 35 to 408 kPa with zero back pressure; (2) increase in effective isotropic confinement from 41 to 203 kPa, followed by the increase in back pressure from 0 to 450 kPa keeping the effective stress constant at 200 kPa; and (3) effective loading from 55 to 413 kPa with a degree of saturation S_r = 40.6%. The chronology of the experimental study is summarized in Table 1. The void ratio was practically constant in all tests (Table 1). The maximum volume-average shear strain γ imposed during torsional resonant testing was in the range of $10^{-6} < \gamma < 10^{-5}$. This is in the same order of magnitude as the maximum volume-average normal strain imposed during flexural testing.

Air-dry test (specimen 1)

Results for the air-dry specimen are presented in Fig. 2. The curve of isotropic confinement σ_o versus axial strain ε_z indicates limited fabric changes, maximum axial strain $\varepsilon_{z\,max}$ =0.11%, and residual axial strain ε_r = 0.02% (Fig. 2A). The predicted behaviour for a simple-cubic (SC) packing is also shown (Santamarina and Cascante 1996; the fitting shear modulus G = 33 GPa; this value is low for quartz, and suggests the higher deformability of nonspherical contacts and differences in fabric). Standard velocity–stress power relations can be verified (e.g., Hardin and Drnevich 1972; Fam and Santamarina 1995) as follows:

$$[8] \qquad V = a(\sigma'_o)^b$$

where a and b are constants, and σ'_o is effective confinement. The curve-fitted exponent for shear waves is b_s = 0.25 during loading and unloading (Fig. 2B). This value suggests one or more of the following situations: conical contacts, contact yield, and fabric densification (Goddard 1990; Cascante and Santamarina 1996). The shear damping coefficient D_S manifested low sensitivity to confinement, especially for σ_o > 150 kPa, and values are similar for loading and unloading (Fig. 2C).

Figure 3A shows that the computed longitudinal wave velocity V_{LF} follows the standard V–σ power relationship with exponent b_{LF} = 0.25. Changes in flexural damping D_F with confinement were minimal (Fig. 3B). The ratio V_{LF}/V_S increased with increasing confinement from 1.42 to 1.46. Poisson's ratio ν for a single-phase isotropic medium can be calculated from V_{LF}/V_S:

$$[9] \qquad \nu = \frac{1}{2}\frac{V_{LF}^2}{V_s^2} - 1$$

The computed Poisson's ratio increases with confinement from 0.01 to 0.07. The longitudinal wave velocity in the rod V_{LF} and the body P-wave velocity are related by

Fig. 3. Dry specimen: flexural excitation. (A) Computed longitudinal velocity V_{LF} vs. confinement. (B) Damping D_F vs. confinement.

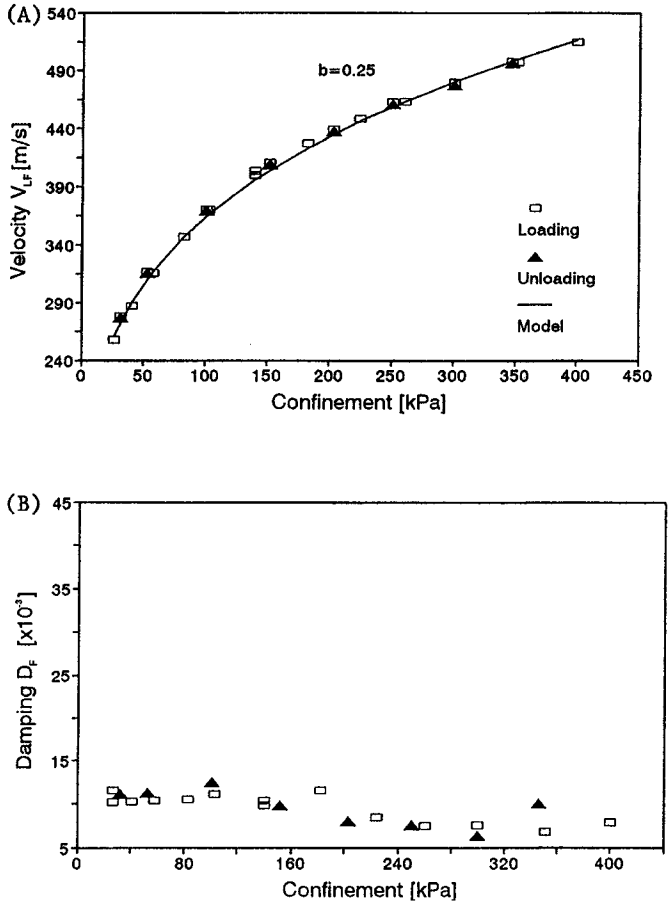

$$[10] \quad V_P = V_{LF}\sqrt{\frac{1-\nu}{(1+\nu)(1-2\nu)}}$$

Finally, the ratio D_F/D_S varied around 1.

Saturated test: no back-pressure (specimen 2)

Results for the saturated specimen with zero back pressure are presented in Fig. 4. The σ_o–ε_z curve suggests limited fabric changes ($\varepsilon_r \approx 0.00\%$, maximum axial strain $\varepsilon_{z\text{-max}} = 0.09\%$; Fig. 4A). The σ_o–ε_z curve for the SC packing is also shown in Fig. 4A. The V_S–σ_o exponent is $b_s = 0.26$ during loading and unloading; V_S is on average 3.4% smaller than that for specimen 1 (Fig. 4B, compare with Fig. 2B). However, the increase in mass due to saturation should have caused a 9.0% decrease in velocity (Table 1). Thus, the shear stiffness G_{max} of specimen 2 ($G_{max} = V^2\rho$) was 11% higher than that for specimen 1. The shear damping coefficient D_S shows low sensitivity to confinement, similar trends for loading and unloading, and values 25% smaller than D_S in the air-dry specimen (Fig. 4C).

Figure 5A shows results for the computed longitudinal wave velocity ($b_{LF} = 0.24$). V_{LF} is smaller than that in the air-dry specimen; this reduction increases with confinement, from 5.4% at 35 kPa to 8.7% at 400 kPa. Note the lack of participation of the bulk stiffness of the fluid. The flexural

Fig. 4. Saturated specimen: torsional excitation (zero back pressure). (A) Stress–strain curve and SC packing model. (B) Shear wave velocity V_S vs. confinement. (C) Damping D_S vs. confinement.

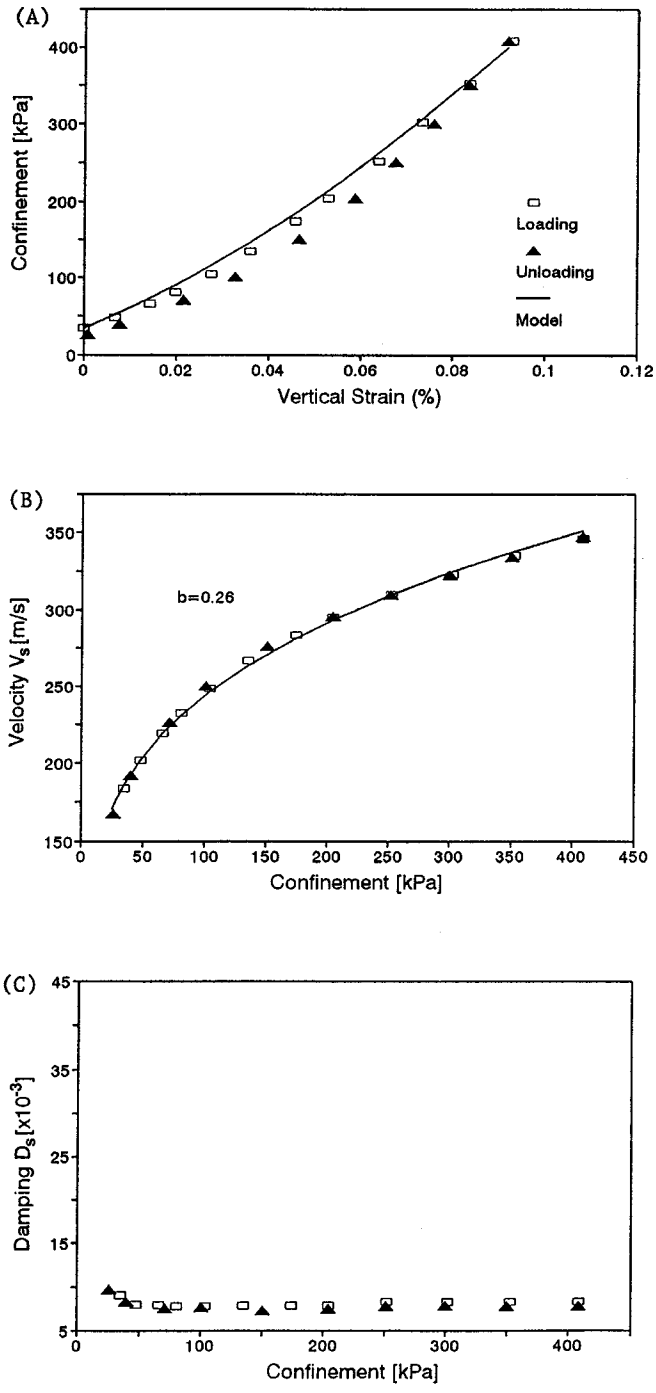

damping D_F decreases with confinement, yet the salient observation is that values of D_F in the saturated specimen are 3.5 times higher than that in the dry specimen (Fig. 5B).

The ratio V_{LF}/V_S decreased with increasing confinement, showing an opposite trend and higher sensitivity to confinement than in the air-dry case (from 1.44 to 1.37). It is inappropriate to compute Poisson's ratio in this case due to the

Fig. 5. Saturated specimen (zero back pressure): flexural excitation. (A) Computed longitudinal velocity V_{LF} vs. confinement. (B) Damping D_F vs. confinement.

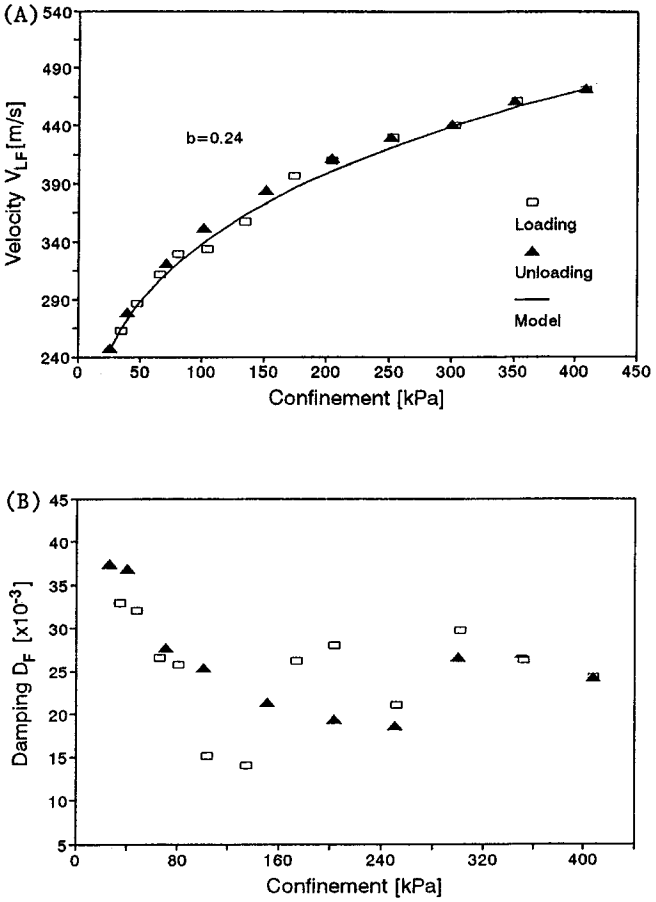

fluid–matrix interaction (Thomsen 1996). The ratio D_F/D_S varied around 3.0.

Saturated test: with back-pressure (specimen 2)

A small amount of entrapped air can drastically reduce the compressibility of fluids. Therefore, back pressure is used in this test to ensure saturation. Following Head (1993), a back pressure of 250 kPa must be applied for 1 week to achieve S_r = 100% when the initial saturation was S_r = 97%; this is a conservative estimate of initial saturation for this specimen. Thus, the test lasted for 9 days to ensure 100% saturation.

The effect of back pressure on the stress–strain response σ_o–ε_z is shown in Fig. 6A (ε_r = 0.01%, $\varepsilon_{z\text{-max}}$ = 0.06%). Differences between loading and unloading are mainly due to time effects. The σ_o–ε_z curve for the SC model is also shown. The V_S–σ_o exponent is b_S = 0.25 for loading and unloading. Values of V_S and D_S during effective isotropic loading are in agreement with the corresponding values measured on the saturated specimen without back pressure (Figs. 6B and 6C compared to Figs. 4B and 4C). V_S and D_S are practically constant while back pressure is increased at constant effective stress σ'_o = 200 kPa. The minor fluctuations are correlated with±5 kPa variations in the effective stress resulting from the independent control of cell and pore pressures. This indicates that neither back pressure nor enhanced saturation affect the phenomena that contribute to shear stiffness or attenuation.

Fig. 6. Saturated specimen: torsional excitation (with back pressure). (A) Stress–strain curve and SC packing model. (B) Shear wave velocity V_S vs. confinement. (C) Damping D_S vs. confinement.

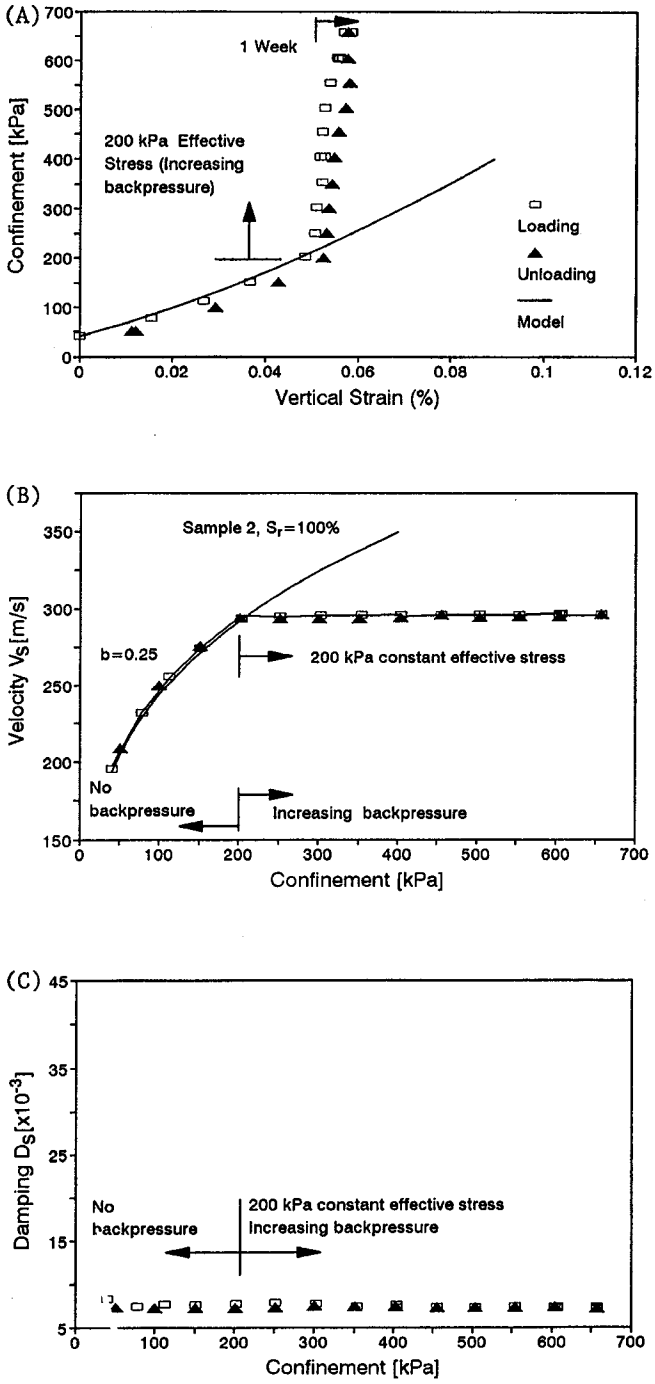

Figure 7 shows results for the longitudinal wave velocity V_{LF} and attenuation D_F computed from flexural excitation during loading and unloading using back pressure (b_{LF} = 0.23). Values of V_{LF} and D_F are also in agreement with the corresponding values measured in the saturated specimen without back pressure (Figs. 5A and 5B).

Fig. 7. Saturated specimen (with back pressure): flexural excitation. (A) Computed longitudinal velocity V_{LF} vs. confinement. (B) Damping D_F vs. confinement.

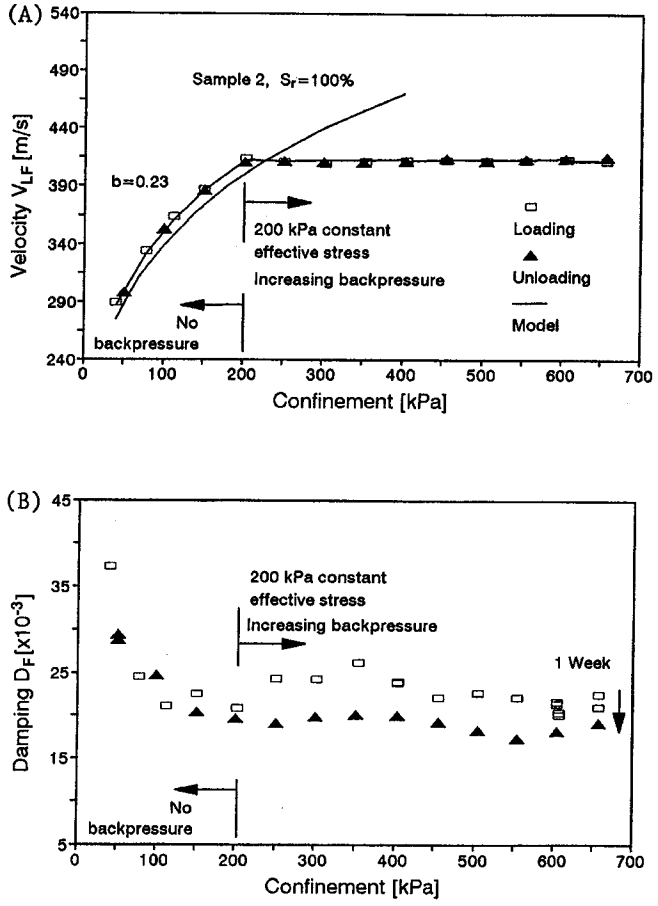

Fig. 8. Partially saturated specimen (S_r = 40.6%): torsional excitation. (A) Stress–strain curve and SC packing model. (B) Shear wave velocity V_S vs. confinement. (C) Damping D_S vs. confinement.

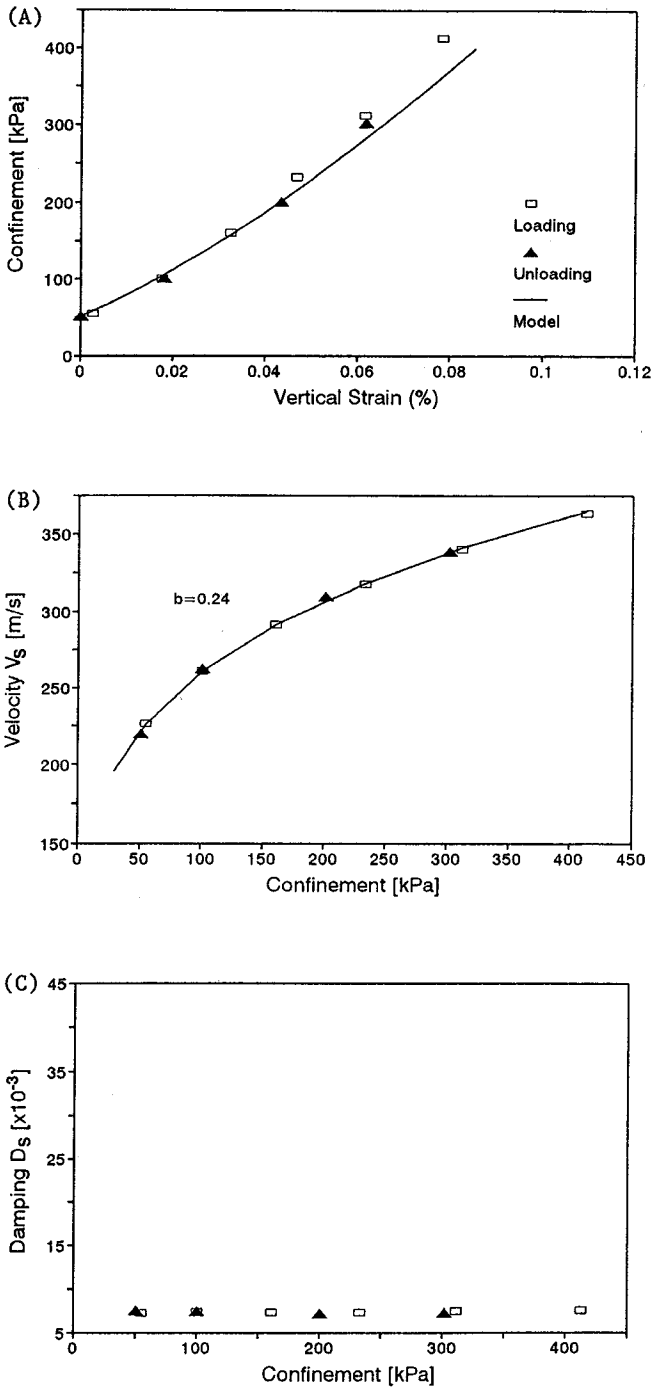

The ratio V_{LF}/V_S decreased with increasing confinement from 1.44 to 1.4, and remained constant during the back-pressurization cycle. The ratio D_F/D_S remained at 2.7 during back pressurization.

Partial saturation test: no back pressure (specimen 2)

The specimen was drained after the completion of the last test, and the isotropic loading–unloading sequence was repeated (S_r = 40.6%). The loading and unloading stress–strain response is almost the same as that observed earlier, reflecting no preloading effects (Fig. 8A; $\varepsilon_r \approx 0.00\%$, $\varepsilon_{z\text{-max}} = 0.08\%$). The computed V_S–σ_o exponent is b_S = 0.24 for loading and unloading. Values of V_S are approximately 5% higher than that in the saturated specimen without back pressure; this increase corresponds to the reduction in mass. Thus, the effect of capillarity on the true effective stress is not important for these large-diameter grains. Shear damping D_S was practically constant and close to the measured values for S_r = 100% with and without back pressure.

The computed longitudinal wave velocity is plotted against confinement in Fig. 9A (b_{LF} = 0.21). Values of flexural damping D_F (Fig. 9B) agree with measured values in the previous two tests with saturated specimens (Figs. 5B, 7B). Overall, the ratios V_{LF}/V_S and D_F/D_S showed similar trends to values observed in the previous tests with saturated specimens.

Observations and discussion

Stress–strain plots

The stress–strain curves for the two specimens were well described by the same regular packing model. The minor

Fig. 9. Partially saturated specimen (S_r = 40.6%): flexural excitation. (A) Computed longitudinal velocity V_{LF} vs. confinement. (B) Damping D_F vs. confinement.

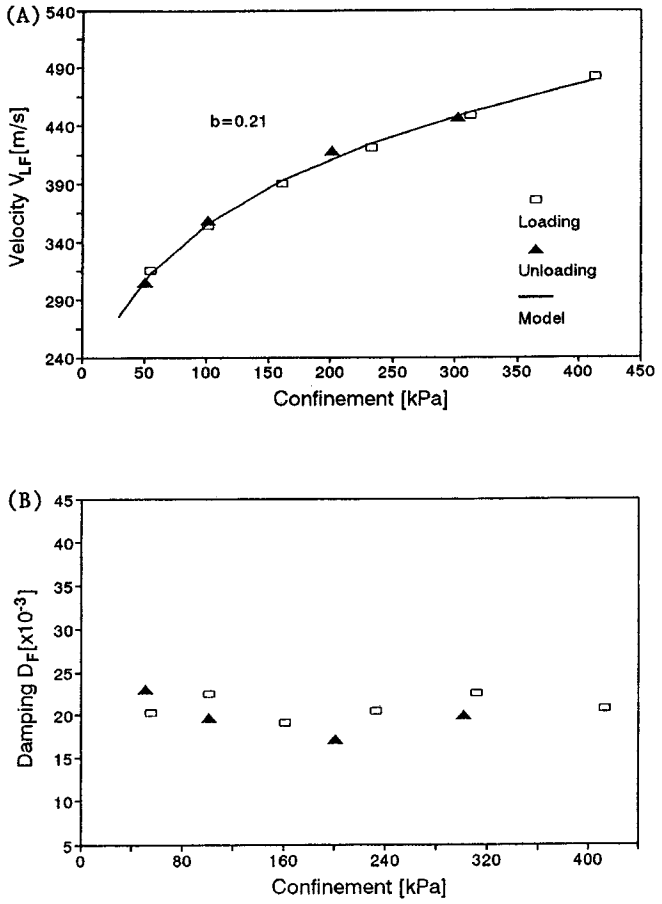

differences in stiffness and residual strain among the two specimens reflects specimen preparation effects.

Torsional excitation: velocity

Shear wave velocity presented consistent paths during loading and unloading under all saturation conditions (Figs. 2B, 4B, 6B, and 8B). The velocity–stress exponent b_S was about the same for the air-dry and wet specimens ($b_s \approx 0.25$). Shear wave velocity was not sensitive to back pressure, as both effective stress and mass density remained constant (Fig. 6B). Capillary forces in the partially saturated test were too small to affect low strain stiffness: based on the formulation by Biarez et al. (1993), the average interparticle force due to capillarity is in the order of 10^{-5} N, whereas the average interparticle force due to confinement is in the order of 10^{-2} N.

Torsional excitation: damping

Shear damping D_S in these dense sands showed low sensitivity to confinement, especially for $\sigma_0 > 100$ kPa (Figs. 2C, 4C, 6C, and 8C). Similar behaviour was observed in steel-sphere specimens by Santamarina and Cascante (1996). It can be argued that in a very dense sand, where the coordination number is high, particle sliding and rotation are limited, restricting the mobilization of friction. Damping decreased 25% from the air-dry case to the wet cases. This may be because of specimen variability (Table 2) or the antilubricant effect of water on nonclean surfaces of sand particles (Feda 1982).

Flexural excitation: velocity

The computed longitudinal wave velocity V_{LF} showed consistent trends for loading and unloading under the four test conditions (Figs. 3A, 5A, 7A, and 9A). The exponent b_{LF} showed rheological effects, decreasing with time from 0.24 to 0.21, suggesting the formation of a more stable fabric as the 2 week long test proceeded (Table 2). The velocity–stress exponent b_{LF} was equal to b_S in the dry specimen, but it was slightly smaller than b_S in the wet tests (10%). Differences between exponents for shear waves and compressional waves of Biot's second type were reported for saturated sands by Richart et al. (1970), but the exponent of the second type of wave was higher than that as a consequence of the fluid–matrix interaction.

The longitudinal wave velocity computed from the flexural mode V_{LF} reflected the stiffness of the soil matrix, like Biot's P-wave of the second type. This is because water can flow from the compression side to the tension side of the specimen faster than half the period of the flexural excitation. Following a simplified pressure diffusion analysis, most of the pressure dissipates when the period of flexural resonance T_{flex} is as follows:

$$[11] \quad T_{flex} > \frac{4gR^2}{kG_sV_s^2}$$

where g is the acceleration due to gravity, R is the radius of the specimen, k is the permeability of the soil, and G_S is the specific gravity of soil particles. For the tested sand, eq. [11] suggests that T_{flex} must be greater than 1/500. Given that resonant frequencies for the flexural mode vary between 50 and 100 Hz (Table 2), it can be concluded that flexural excitation tested primarily the stiffness of the skeleton.

The velocity V_{LF} decreased from the air-dry to the saturated conditions (5.4–8.7%). The expected decrease due to the increase in mass density should have been 3.7%, estimated after correction for higher stiffness of specimen 2. Thus, it appears that the drag of the water in the pores reduced the value of V_{LF} in the saturated specimen, and this effect increased with increasing confinement, which implies higher frequencies. On the other hand, the increase in V_{LF} from the fully saturated to the partially saturated case (S_r = 40.6%) was independent of confinement and in agreement with the expected increase due to the change in mass density (~5%). This suggests that the drag effect of the water was also present at S_r = 40.6%, with the same magnitude as that for S_r = 100%. Furthermore, given that the longitudinal wave velocity V_{LF} was governed by the stiffness of the matrix, it should not be sensitive to back pressure, in agreement with experimental results (Fig. 7A).

Flexural excitation: damping

Damping D_F presented a significant increase from the air-dry to the wet cases (Figs. 3B, 5B, 7B, and 9B). This shows the importance of local flow and the relative movement of the water with respect to the soil skeleton. Hence, flexural excitation of saturated specimens provides evidence

of high-energy dissipation mechanisms which are characteristic in Biot's second type of compressional wave. Because small volumes of water can be mobilized at contacts, local flow loss can also justify high losses in partially saturated specimens. D_F displayed clearer rheological stabilization effects than D_S (Figs. 6C, 7B). Therefore, the rheological stabilization of the soil skeleton affects the local flow mechanism.

Compressional wave velocity V_P, Poisson's ratio ν, and ratios V_{LF}/V_S and D_F/D_S

Equations [9] and [10] are valid when the porous medium behaves like an equivalent isotropic and elastic media. If the velocity of the second type of wave is used in eq. [9] the computed Poisson's ratio would be negative.

The Poisson's ratio computed with eq. [9] for the air-dry sand is small ($\nu < 0.07$). This is the case of isotropic regular packings subjected to small-strain perturbation at constant fabric (no change in coordination number, void ratio, and distribution of contact forces) (Petrakis and Dobry 1987; Santamarina and Cascante 1996). Analytical solutions based on conical or Hertzian contact predict Poisson's ratio independent of the state of stress. Yet, experimental results with the air-dry specimen show that small-strain Poisson's ratio increases with confinement. Theoretical results presented by Wang and Nur (1992) agree with these observations. Their model applies to a homogeneous and isotropic random packing of elastic spheres, whereby neighboring spheres are firmly bonded across small, flat, and circular regions of the same average radius.

The ratio V_{LF}/V_S in the air-dry specimen increased with confinement and reached a value of 1.46 at 400 kPa. This is close to the value of $V_P/V_S = 1.49$ measured for quartz (Eastwood and Castagna 1987). The ratio V_P/V_S tends to the ratio V_{LF}/V_S when $n \approx 0$. In the case of the wet specimens, the ratio V_{LF}/V_S decreases with confinement because $b_{LF} < b_S$ due to the fluid–matrix viscous interaction at higher frequencies (Table 2). Murphy (1982) observed similar behaviour for the V_P/V_S ratio for fully saturated sandstones.

The ratio D_F/D_S was about 1.0 for the dry specimen and varied within $D_F/D_S = 3.5 \pm 1.0$ for the wet specimens. This significant increase in attenuation reflects the effect of the local flow mechanism in the compressional excitation of saturated particulate materials. Thus, attenuation measurement could be used to infer wet–dry conditions in granular materials as suggested by Murphy (1982) in the context of rocks.

Conclusions

Multimode excitation testing augments the characterization of particulate materials. Flexural and torsional resonance are suitable to study wave propagation characteristics in particulate materials in a frequency range which is applicable to near-surface, high-resolution applications (between 50 and 200 Hz). The standard torsional resonant column device and test procedures were modified to permit the flexural excitation of the specimen.

The flexural excitation of saturated particulate media may not be affected by the stiffness of the fluid. This depends on the size of the specimen, its permeability, and the stiffness of the skeleton. Membrane compliance in flexible-wall cells permits the pore pressure to decay towards the membrane in longitudinal and flexural waves (transverse flow in both excitations). The effect of membrane compliance is maximized at low frequencies. In this case, the stiffness of the fluid does not contribute to the longitudinal wave velocity. Flexural excitation highlights losses due to fluid–skeleton interaction.

Longitudinal and shear wave velocities are affected by the state of stress, but show little sensitivity to the stress history (fresh laboratory specimen made of dense quartzitic sand). Neither back pressure nor enhanced saturation affects the phenomena that contribute to stiffness in either flexural or transverse excitation mode. The exponent in velocity–stress relations is sensitive to rheological fabric stabilization.

The damping coefficient D_S showed little sensitivity to confinement in these dense specimens ($D_r = 100\%$). The high coordination number and rotational frustration restricted the mobilization of interparticle friction and reduced the stress dependency of hysteretic attenuation.

The computed longitudinal wave velocity V_{LF} changed under saturation more than implied by the change in density. Fluid–matrix interaction increases energy losses. Local flow remains active at partial saturation; this loss mechanism decays at low saturation levels as the water menisci at contacts vanish.

The ratio D_F/D_S showed a significant increase from the air-dry condition ($D_F/D_S \approx 1$) to the saturated and partially saturated conditions ($D_F/D_S = 3.5 \pm 1.0$). Thus, attenuation provides information independent of velocity with respect to the saturation condition of the medium.

Acknowledgments

This research is part of a study on wave–geomedia interaction and applications. Support was provided by the Natural Sciences and Engineering Research Council of Canada and the University of Waterloo ID Program.

References

Biarez, J., Fleureau, J.M., and Taibi, S. 1993. Constitutive model for unsaturated granular media. *In* Powders and grains. *Edited by* C. Thornton. A.A. Balkema, Rotterdam, The Netherlands, pp. 51–58.

Cascante, G. 1996. Low strain measurements with mechanical waves in geomaterials—experimental micromechanics. Ph.D. thesis, University of Waterloo, Waterloo, Ont.

Cascante, G., and Santamarina, J.C. 1996. Interparticle contact behaviour and wave propagation. Journal of Geotechnical Engineering, ASCE, **122**(10): 831–839.

Cascante, G., and Santamarina, J.C. 1997. Low strain measurements using random noise excitation. Geotechnical Testing Journal, **20**(1): 29–39.

Domenico, S.N., and Danbom, S.H. 1987. Shear-wave technology in petroleum exploration—past, current, and future. *In* Shear-wave exploration. Geophysical development series. Vol. 1. *Edited by* S.H. Danbom and S.N. Domenico. Society of Exploration Geophysicists, Tulsa, Okla., pp. 3–18.

Dutta, N.C. 1987. Geopressure. Geophysics Reprint Series No.7. Society of Exploration Geophysicists, Tulsa, Okla., pp. 227–229.

Eastwood, R.L., and Castagna, J.P. 1987. Interpretation of Vp/Vs ratios from sonic logs. *In* Shear-wave exploration. Geophysical development series. Vol. 1. *Edited by* S.H. Danbom and S.N. Domenico. Society of Exploration Geophysicists, Tulsa, Okla., pp. 139–153.

Fam, M., and Santamarina, J.C. 1995. Study of complementary mechanical and electromagnetic wave measurements in an oedometer. Geotechnical Testing Journal, **18**(3): 307–314.

Feda, J. 1982. Mechanics of particulate materials—the principles. Developments in Geotechnical Engineering, Vol. 30. Elsevier-Academia, New York.

Fratta, D., and Santamarina, J.C. 1996. Wave propagation in soils: multi-mode, wideband testing in a waveguide device. Geotechnical Testing Journal, **19**(2): 130–140.

Futterman, W.I. 1962. Dispersive body waves. Journal of Geophysical Research, **67**(13): 5279–5291.

Goddard, J.D. 1990. Nonlinear elasticity and pressure-dependent wave speeds in granular media. Proceedings of the Royal Society of London, Series A, **430**: 105–131.

Hardin, B.O., and Drnevich, V.P. 1972. Shear modulus and damping in soils: measurements and parameter effects. Journal of the Soil Mechanics and Foundations Division, ASCE, **98**: 603–624.

Head, K.H. 1993. Manual of soil laboratory testing. Vol. 3. Effective stress tests. Pentech Press, London.

Kolsky, H. 1963. Stress waves in solids. Dover Publications Inc., New York.

Murphy, W.F. 1982. Effects of partial water saturation on attenuation in massilon sandstone and Vycor porous glass. Journal of the Acoustical Society of America, **71**(6): 1458–1467.

Petrakis, E., and Dobry, R. 1987. Micromechanical modeling of granular soil at small strain by arrays of elastic spheres. Department of Civil Engineering, Rensselaer Polytechnic Institute, Troy, N.Y., Report CE-87-02, pp. 90–115.

Richart, F.E., Jr., Hall, J.R., and Woods, R.D. 1970. Vibration of soils and foundations. Prentice-Hall, Inc., Englewood Cliffs, N.J.

Santamarina, J.C., and Cascante, G. 1996. Stress anisotropy and wave propagation: a micromechanical view. Canadian Geotechnical Journal, **33**(5): 770–782.

Thomsen, L. 1996. Poisson was not a rock physicist, either! The Leading Edge, **15**: 852–855.

Toksöz, M.N., Chen, C.H., and Timur, A. 1976. Velocities of seismic waves in porous rocks. Geophysics, **44**: 621–645.

Wang, Z., and Nur, A. 1992. Elastic wave velocities in porous media: a theoretical recipe. Seismic and Acoustic Velocities in Reservoir Rocks, Vol. 2, pp. 1–35.

White, J.E. 1975. Computed seismic speeds and attenuation in rocks with partial gas saturation. Geophysics, **40**: 224–232.

Winkler, K., and Nur, A. 1982. Seismic attenuation: effects of pore fluids and frictional sliding. Geophysics, **47**: 1–15.

Appendix 1: List of symbols

a, b: constants

b_S, b_{LF}, b_P: velocity–stress exponents for shear, longitudinal, and compressional waves, respectively

d: specimen diameter

e: void ratio

e_{max}, e_{min}: maximum and minimum void ratios, respectively

f: frequency of excitation (Hz)

g: acceleration due to gravity (cm/s^2)

h_a: equivalent height of the calibration mass

h_b: height of the top bar of the calibration specimen

$h0_i$, $h1_i$: heights at bottom and top, respectively, of added masses m_i (cm)

k: permeability of the soil (cm/s)

m_T: mass of the system (m_i added masses at the top of the specimen) (kN s^2/m)

$volt_{pk}$: maximum output voltage of the accelerometer (mV)

x: elevation from the base of the specimen

x_{accel}: elevation of the accelerometer

y: horizontal displacement of the specimen

y_{ci}: center of gravity of mass m_i, measured from the top of the specimen (cm)

y_{meas}: maximum flexural displacement of the specimen

A: cross-sectional area

D_S, D_F: damping coefficients for torsional and flexural vibration modes, respectively

D_P: compressional damping

D_r: relative density

D_{50}: diameter for 50% passing

E, E_{flex}: Young's modulus and Young's modulus from flexural excitation, respectively (kPa)

I_b: area moment of inertia of the specimen (cm^4)

I_y: area moment of inertia

I_{yi}: area moment of inertia of mass m_i (cm^4)

I_{yp}: area moment of inertia of the driving plate

G, G_{max}: shear modulus (kPa), maximum shear modulus (kPa)

G_S: specific gravity of soil particles

J_U: maximum internal potential energy

J_T: maximum kinetic energy

L: length of the specimen (cm)

N: total number of masses added at the top of the specimen

R: radius of the specimen (cm)

S: sensitivity of the accelerometer (mV/g)

S_r: degree of saturation

T_{flex}: period of flexural resonance

V: velocity

V_S, V_{LF}, V_P: shear, longitudinal, and compressional wave velocities, respectively (m/s)

α: constant

$|\Delta vol|$: volume change of the specimen due to tension or compression

ε_{avg}: volume-average axial strain for flexural excitation

ε_r: residual axial strains caused by isotropic loading

ε_z: axial strain

$\varepsilon_{z\text{-}max}$, ε_{max}: maximum axial strains caused by flexural excitation and isotropic loading, respectively

γ: shear strain

ρ: mass density of the specimen (kN s^2/m^4)

σ: stress

σ_o: isotropic confinement (kPa)

σ'_o: effective confinement

ν: Poisson's ratio

ω_f, ω_t: undamped flexural and torsional natural circular frequencies, respectively (rad/s)

ω_1, ω_2, ω_3: resonant frequency of the calibration specimen alone, with the added calibration mass at the top, and with a changed vertical position of the driving plate, respectively

Appendix 2: Relevant equations for the analysis of flexural excitation

Resonant Frequency: Rayleigh's method

The mode shape for the horizontal displacement y of the specimen at elevation x is assumed to be a third-order polynomial:

$$[A1] \quad y(x) = a_0 + a_1 x + a_2 x^2 + a_0 x^3$$

At the lower plate (corresponding to elevation $x = 0$) the displacement and the tangent are $y(0) = 0$ and $y'(0) = 0$, respectively. Hence, $a_0 = 0$ and $a_1 = 0$. Neglecting the moment at the top end $x = L$, $Eiy''(L) = 0$. Then, eq. [A1] becomes

$$[A2] \quad y(x) = \alpha x^2 [3L - x] \qquad \text{for} \quad x < L$$

where α is a constant given by $\alpha = (a_2/3L)$. Equation [A2] also represents the elastic deformation of a cantilever beam with a transverse load at the free end. The horizontal displacement of rigid masses placed above the specimen are estimated from the horizontal displacement $y(L)$ and the tangent $y'(L)$ at the top of the specimen:

$$[A3] \quad y(x) = \alpha L^2 [2L + 3(x - L)] \qquad \text{for} \qquad x < L$$

The maximum internal potential energy J_U (extreme deformation) is computed by taking into consideration only the internal energy in the deformed specimen:

$$[A4] \quad J_U = \frac{1}{2} EI_b \int_0^L y''(x)^2 \, dx, \qquad J_U = 6EI_b \alpha^2 L^3$$

where E is the Young's modulus, and I_b is the area moment of inertia. The maximum kinetic energy J_T (maximum velocity) is computed by presuming harmonic oscillation with frequency ω_f. The component for the specimen is

$$[A5] \quad J_{T1} = \frac{1}{2} \rho \omega_f^2 A \int_0^L y(x)^2 \, dx, \qquad J_{T1} = \frac{33}{70} \omega_f^2 \alpha^2 L^6 m_T$$

where A is the cross-sectional area. The kinetic energy for a concentrated mass added at a distance h above the specimen can be evaluated using eq. [A3] with $h = (x - L)$:

$$[A6] \quad J_{T2} = \frac{1}{2} m [\alpha L^2 (2L + 3h)]^2$$

$$J_{T2} = m\alpha^2 L^6 \left[2 + 6\frac{h}{L} + \frac{9}{2}\left(\frac{h}{L}\right)^2 \right]$$

Finally, the circular resonant frequency for the flexural mode is computed by equating the maximum internal potential energy J_U and the maximum kinetic energy $J_{T1} + J_{T2}$:

Fig. A1. Calibration setup for flexural excitation.

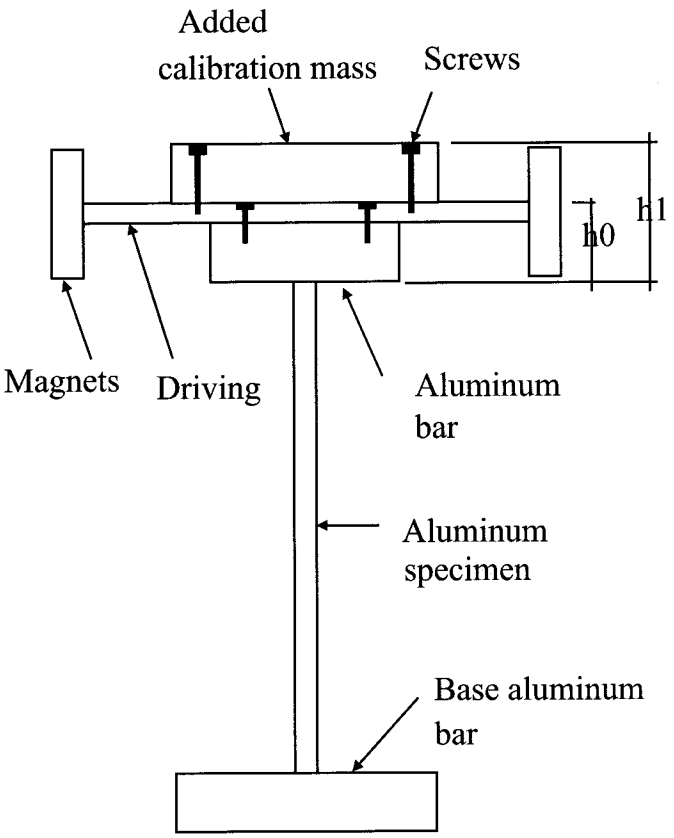

$$[A7] \quad \omega_f^2 = \frac{3EI_b}{\left\{ \frac{33}{140} m_T + m \left[1 + 3\frac{h}{L} + \frac{9}{4}\left(\frac{h}{L}\right)^2 \right] \right\} L^3}$$

The previous equation can be extended to N masses m_i. Each mass has a mass density ρ_i and cross-sectional area A_i, and is uniformly distributed from height $h0_i$ to $h1_i$ (measured from the top end of the specimen, Fig. A1). Then

$$[A8] \quad \omega_f^2 = \frac{3EI_b}{\left[\frac{33}{140} m_T + \sum_{i=1}^{N} m_i \, h(h0_i, h1_i) \right] L^3}$$

where

[A9]

$$h(h0_i, h1_i) = 1 + \frac{3(h0_i + h1_i)}{2L} + \frac{3(h0_i^2 + h0_i h1_i + h1_i^2)}{4L^2}$$

Equation [A9] can be written in terms of the centre of gravity y_{ci} and the mass moment of inertia I_{yi} of each mass m_i:

$$[A10] \quad h(y_{ci}, I_{yi}) = 1 + \frac{3y_{ci}}{L} + \frac{9}{4L^2}\left[\frac{I_{yi}}{m_i} + y_{ci}^2 \right]$$

Average axial strain

The axial strain at elevation x and at distance r from the neutral plane is

$$[A11]\quad \varepsilon(x, r) = \frac{d^2 y}{dx^2} \cdot r = 6 \cdot \alpha(L - x) \cdot r$$

For the circular column with radius R and total volume V, the average strain is defined in terms of the tension or compression side as

$$[A12]\quad \varepsilon_{avg} = \frac{1}{V/2} \int_{V/2} \varepsilon(x, r) \cdot dA \cdot dx$$

Hence,

$$[A13]\quad \varepsilon_{avg} = \frac{2}{V} \int_0^L \int_0^R 6 \cdot \alpha(L - x) \cdot r \cdot \left(2\sqrt{R^2 - r^2} \cdot dr \right) \cdot dx$$

$$\varepsilon_{avg} = \frac{4}{\pi} \cdot R \cdot L \cdot \alpha$$

The value of α is computed from eq. [A3] with the maximum flexural displacement y_{meas} measured at the elevation of the accelerometer x_{accel}:

$$[A14]\quad \alpha = \frac{y_{meas}}{L^2 [2L + 3(x_{accel} - L)]}$$

The average strain can be related to the maximum strain experienced at the lower edge of the specimen $\varepsilon_{max} = 6 \cdot \alpha \cdot L \cdot R$. Replacing in eq. [A13],

$$[A15]\quad \varepsilon_{avg} = \frac{2}{3\pi} \varepsilon_{max}$$